

<https://doi.org/10.1038/s43246-024-00499-z>

# Narrow bandgap silver mercury telluride alloy semiconductor nanocrystal for self-powered midwavelength-infrared photodiode

Check for updates

Haemin Song<sup>1,4</sup>, So Young Eom<sup>1,4</sup>, Gahyeon Kim<sup>1,4</sup>, Yoon Seo Jung<sup>1</sup>, Dongsun Choi<sup>1</sup>, Gundam Sandeep Kumar<sup>1</sup>, Jin Hyeok Lee<sup>1</sup>, Hyeong Seok Kang<sup>1</sup>, Jiyeon Ban<sup>1</sup>, Gyeong Won Seo<sup>2,3</sup>, Sungmin Hong<sup>1</sup>, Sooho Bae<sup>1</sup>, Gyu Weon Hwang<sup>1,2</sup>, Woong Kim<sup>1,3</sup> & Kwang Seob Jeong<sup>1</sup> ✉

Infrared colloidal quantum dots (CQDs) have been of interest due to their low-cost fabrication and facile wavelength tunability for various infrared optoelectronic applications. Recently, the mid-wavelength infrared (MWIR) quantum dot sensor has been successfully realized by forming a photodiode via a post-chemical treatment method. Controlling the doping density of the quantum dot solid and engineering the device structure require an extremely sophisticated technique, which hinders consistent doping density and restricts further development in understanding the fundamental photophysics and manufacturing process. Here, we report an air-stable and highly reproducible MWIR CQDs photodiode by incorporating synthesized p-doped Ag-HgTe colloidal nanocrystals (NCs). The Ag-HgTe alloy NCs allow clearly defined p-doped QDs layers, leading to uniform dopant distribution and the ease of engineering device fabrication. By optimizing the doping density, we achieved an average noise equivalent temperature difference of below 10 mK at 78 K with the self-powered MWIR photodiode sensor.

With a rising demand for mid-wavelength infrared (MWIR) detectors in defense, agriculture, telecommunication, advanced transportation, biomedical imaging, and environmental fields, reducing the cost of mid-infrared optoelectronics has come to the fore since infrared materials cost several times more than visible materials<sup>1–6</sup>. Following the epitaxially grown materials and superlattice structures, colloidal quantum dots (CQDs) have rapidly emerged as a next-generation infrared-sensitive material due to their excellent properties, such as low-cost manufacturing process with no need for the high-temperature procedure, wavelength tunability, facile synthesis, and solution processibility<sup>7–22</sup>.

In a decade, CQDs-based detectors have been progressively investigated by the lead of Hg-based CQDs, which have a narrow bulk bandgap energy suitable for MWIR<sup>23</sup>. Following the first report on the HgTe CQDs-based photoconductive MWIR detector, Guyot-Sionnest and co-workers demonstrated the photovoltaic HgTe CQDs-based mid-IR detector<sup>24</sup>. The p-n junction was built between HgTe (n-type) and Ag<sub>2</sub>Te (p-type) CQDs

layers, where the solid-state cation exchange process with Hg cations on the QDs film state controlled the p-doping level of the Ag<sub>2</sub>Te CQDs layer<sup>25</sup>. The photodiode structure suppressed noise and reached close to the background limited infrared photodetection (BLIP), exhibiting commercially comparable performance. The accomplishment in photovoltaic structure encouraged the CQDs-based detector community, followed by several studies introducing electron/hole transport layers and novel photonic structures to overcome the limitations and achieve suitable band alignment and enhanced absorbance.

However, the following research has been limited to the early HgTe CQDs/solid-state cation-exchanged Ag<sub>2</sub>Te CQDs structures, focusing on the supplementary materials for further improvement rather than the chemical properties of quantum dots that directly affect the formation of the appropriate p-n junction<sup>24,26,27</sup>. Recently, Tang and co-workers demonstrated a p-n homojunction by utilizing the solution-state ligand exchange process on the HgTe CQDs to control n-/p-type characteristics, which

<sup>1</sup>Department of Chemistry, Korea University, Seoul 02841, Korea. <sup>2</sup>Center for Neuromorphic Engineering, Korea Institute of Science and Technology, Seoul 02792, Korea. <sup>3</sup>Department of Materials Science and Engineering, Korea University, Seoul 02841, Korea. <sup>4</sup>These authors contributed equally: Haemin Song, So Young Eom, Gahyeon Kim. ✉e-mail: [kwangsejeong@korea.ac.kr](mailto:kwangsejeong@korea.ac.kr)

revealed a comparable performance even at 300 K resulting from the enhanced infrared absorption due to higher packing density of homo-junction. Other studies showed the solution state ligand exchange increased the carrier mobility of CQDs up to 1–4 orders of magnitude<sup>12,28,29</sup>. This infers that chemically modifying the CQDs nature plays a significant role in determining the performance, suggesting the need for further study of chemical control of the CQDs.

While the HgTe CQDs have been continuously investigated in various ways, such as doping density and carrier mobility<sup>26,30</sup>, the research has lacked the p-type CQDs despite the significance of their doping state in forming the built-in potential. Although widely used Hg-doped Ag<sub>2</sub>Te CQDs have shown promising performance as a p-doped material, it has suffered to advance towards further optimization and application since the solid-state post-chemical treatment necessitates extremely sophisticated process with an optimum concentration for doping density control of p-doped material. Moreover, the solid-state cation exchange process should always be carried out after n-doped QDs film fabrication for forming the adequate p-n junction due to the different doping densities within the layer. Therefore, addressing this issue will give enormous freedom in device fabrication.

Here, we present an air-stable, high-resolution mid-IR CQD photodiode by developing p-doped Ag-HgTe alloy NCs. Under the p-doped Ag-HgTe NCs that eliminate the need for solid-state cation exchange treatment, the doping density of the p-doped QDs layer was successfully controlled. The p-doped Ag-HgTe NCs were optimized by changing the amount of the silver dopant and the surface ligands to ideally align the energy band with the n-HgTe NCs and form uniform, less aggregated film. As a result, the mid-IR CQDs photodiodes optimized here exhibit a high temperature resolution, noise equivalent temperature difference (NETD), of 3 mK under zero bias.

## Results and discussion

### Characterization of the nanocrystals

Figure 1 provides the physical properties of the Ag-HgTe and HgTe NCs. For the p-type material, previous reports on the mid-IR CQDs photovoltaic detectors have mainly exploited the solid-state cation exchange method by applying the mercury precursor solution onto the Ag<sub>2</sub>Te CQDs for forming the p-type Hg-doped Ag<sub>2</sub>Te CQDs layers<sup>25</sup>. Although the post-cation exchange method exhibited a high detectivity comparable to the commercial detectors, there has been the risk of film crack and restricted applicability of p-type material. To overcome the limitations, we synthesized the Ag-HgTe alloy NCs.

Briefly, metal precursors of AgCl(s) and HgCl<sub>2</sub>(s) were simultaneously added into the oleylamine (OLAM) solvent and degassed under a vacuum to remove the water and oxygen. After degassing, the temperature of the solution was set to 97 °C, followed by quickly injecting the trioctylphosphine-tellurium (TOP-Te) solution into the flask. The reaction proceeded for the desired reaction time, and the reaction was quenched in the ice bath by injecting additional ligands, TOP and 1-dodecanethiol (DDT).

Figure 1a shows the Fourier transform-infrared (FT-IR) absorption spectra of the Ag-HgTe and HgTe NCs. The sharp peaks at 2922 cm<sup>-1</sup> correspond to the vibrational mode of C-H stretching in the DDT, TOP, and OLAM ligands passivating the nanocrystal surface. The bandgap excitonic peaks of the Ag-HgTe and HgTe NCs are observed at ~3600 and ~3000 cm<sup>-1</sup>. The less distinct bandgap absorption feature of the Ag-HgTe NCs is attributed to the mixing with C-H vibrational modes (asymmetric and symmetric) of the surface ligands. The bandgap feature clearly appears after the ligand is exchanged to the shorter (Supplementary Fig. 1). The bandgap absorption of HgTe NCs redshifted to 2000 cm<sup>-1</sup> by treating 1,2-ethanedithiol (EDT) ligands, which is suitable for detecting the mid-IR. This redshift is caused by the overlap of wavefunctions of the NCs as the interdot distance decreases.

The X-ray diffraction (XRD) pattern indicates that the crystal structure of the HgTe NCs is a zinc-blende cubic phase with distinct (111), (220), and

(311) facets (Fig. 1b). The lattice spacing of 0.37 nm corresponds to the (111) facet plane, which corresponds to the zinc-blende structure of HgTe (Fig. 1b). The XRD pattern of the Ag-HgTe NCs demonstrates the Ag doping of HgTe NCs, showing the major peaks related to the cubic HgTe and minor peaks related to the monoclinic Ag<sub>2</sub>Te. The zinc-blende peaks of Ag-HgTe are slightly shifted to a lower 2-theta value, which indicates that the doped NCs are expanded to a higher lattice parameter by incorporating Ag into the HgTe lattice (Fig. 1b, Supplementary Fig. 2). The lattice parameters of Ag-HgTe and HgTe NCs were calculated by Bragg's law, which resulted in 6.452 nm for the lattice parameter of Ag-HgTe NCs, larger than that of HgTe NCs (6.432 nm). The XRD pattern of Ag-HgTe NCs in Fig. 1b is associated with 10.5% of Ag doping, which will be explained below, and it is compared with that of 2.0% Ag-doped HgTe NCs in Supplementary Fig. 3.

X-ray photoelectron spectroscopy (XPS) spectra of HgTe and Ag-HgTe NCs also show the difference in binding energy attributed to the Ag dopant (Fig. 1c). Two Hg 4f peaks, which indicate Hg-Te and Hg-S binding states<sup>31</sup>, are shifted to 0.47 eV lower binding energy in Ag-HgTe NCs compared to HgTe NCs. Likewise, Te 3d peaks of Ag-HgTe NCs are also located at lower binding energy than those of HgTe NCs (Supplementary Fig. 4). This demonstrates that the chemical interaction between Hg cations and Te anions was altered due to the Ag incorporation<sup>32</sup>.

Transmission electron microscopy (TEM) images show the elongated morphology of Ag-HgTe NCs, different from the tetrahedral shape of HgTe NCs (Fig. 1d, Supplementary Fig. 5). The average length and width are ~11.2 and ~4.5 nm, respectively, indicating the aspect ratio of ~2.5 (Supplementary Fig. 6). It is well known that the (111) facet plays a dominant role in forming the elongated morphology, and the nanowires grow in the (111) facet in general<sup>33</sup>. While the fast Fourier transform (FFT) analysis of HgTe NCs evenly shows three interplanar distances associated with main facets of cubic HgTe (3.7 Å, 2.3 Å, and 1.9 Å corresponding to (111), (220), and (311) facet, respectively), that of Ag-HgTe NCs reveals that the interplanar distance of 3.7 Å corresponding to the (111) facet was observed in the Ag-HgTe NCs, as proven in TEM images (Supplementary Fig. 7). In addition, the TEM image of Ag-HgTe NCs accompanied by energy dispersive spectrometry (EDS) mapping demonstrates the uniform distribution of Ag, Hg, and Te atoms (Supplementary Fig. 8).

Considering the valence electrons of the Hg and Ag atoms, which are 2 and 1, respectively, replacing an Hg atom with an Ag atom causes an electron-deficient bonding, leading to the p-doped character. To confirm the doping character, the field effect transistor measurement was conducted (Supplementary Fig. 9). The conductance of Ag-HgTe NCs decreases as the gate potential increases, proving the p-type character of Ag-HgTe NCs. In contrast, HgTe NCs exhibit the opposite behavior, the characteristic of n-type material<sup>34</sup>. Thus, HgTe and Ag-HgTe NCs are suitable for n- and p-type material for photodiodes, respectively.

### Fabrication of the HgTe-based CQDs MWIR detector

The structure of the fabricated MWIR NCs photodiode is sapphire/ITO (indium tin oxide)/HgTe/Ag-HgTe/Au. Its schematic diagram is illustrated in Fig. 2a. Sapphire substrate and ITO electrode were used due to their relatively high transparency in the infrared region. The HgTe and Ag-HgTe NCs layers were deposited with the layer-by-layer (LBL) method. The HgTe film was treated with the EDT/HCl to enhance the n-type character. Supplementary Fig. 10 shows the image of the HgTe NCs layer deposited films with a thickness of 440 nm using the cross-sectional focused ion beam (FIB). It indicates that the final thickness of the n- and p-type layers are 440 and 45 nm, respectively, shown in the FIB image of the device (Fig. 2b). The cross-section of the NCs layer deposited by the LBL method appears extremely smooth, which enhances the device performance.

Since the work function of ITO has been reported to be between 4.5 and 4.7 eV<sup>35</sup>, it is compatible with the conduction band position of HgTe NCs (4.5 eV)<sup>36</sup>, minimizing barriers for electron transport and working as an appropriate electronic contact. Figure 2c shows the band alignment of the HgTe CQDs detector, which is analyzed by ultraviolet photoelectron spectroscopy (UPS) (Supplementary Fig. 11). The conduction band offset

**Fig. 1 | The optical and physical properties of the nanocrystals.** **a** FT-IR absorption spectra of Ag-HgTe and DDAB-treated HgTe NCs. **b** XRD patterns of Ag-HgTe and HgTe NCs with the references of cubic HgTe and monoclinic Ag<sub>2</sub>Te and **c** XPS spectra of Hg 4f of HgTe and Ag-HgTe NCs. **d** TEM images of Ag-HgTe NCs (scale bar = 10 nm).

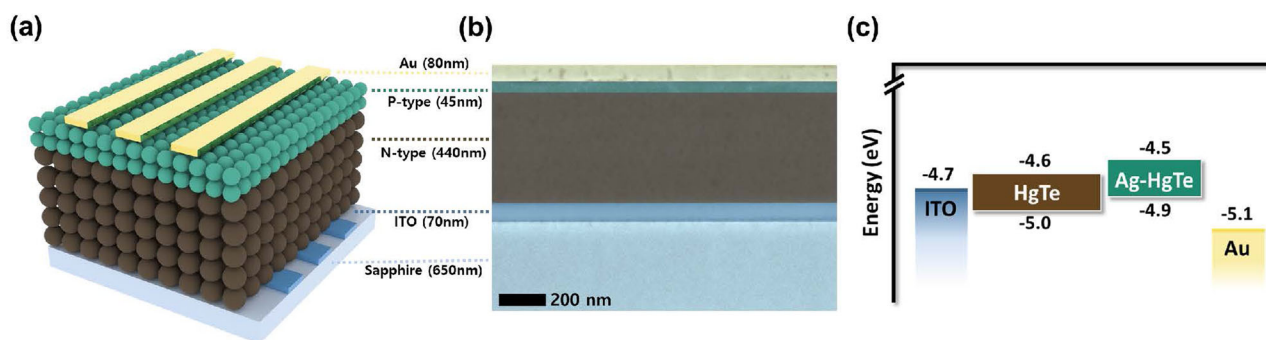
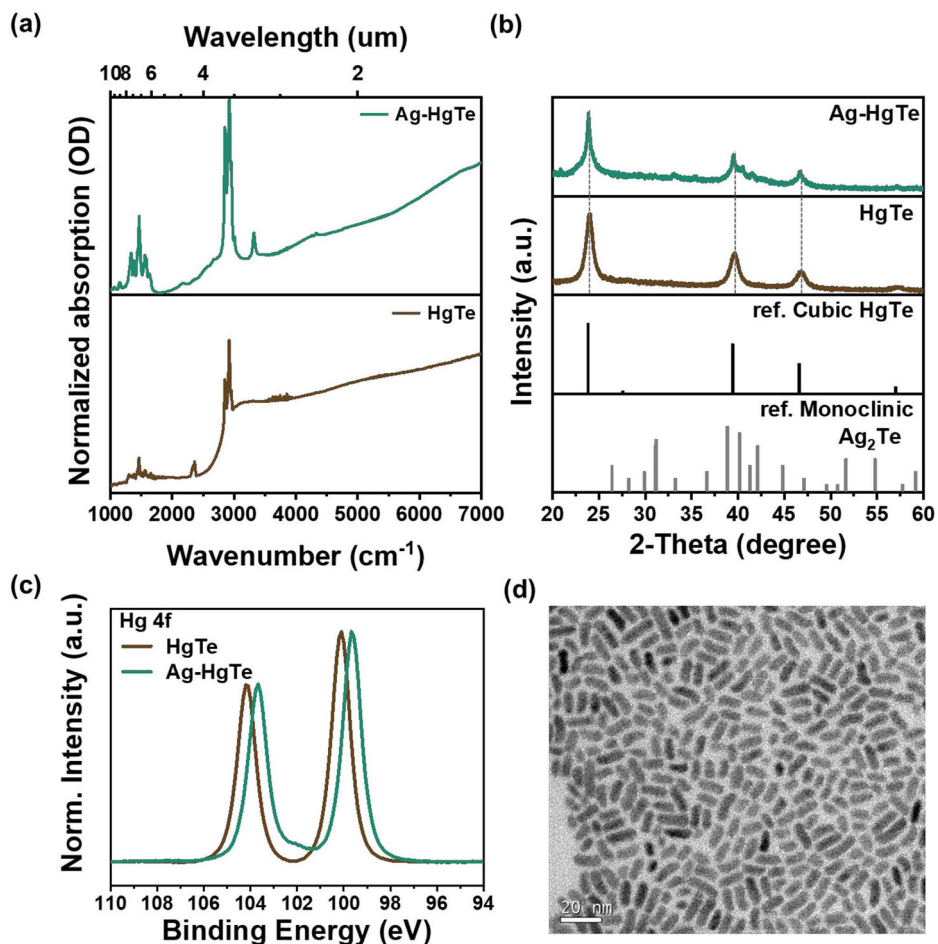


**Fig. 2 | The device structure of the fabricated detector.** **a** Schematic of sapphire/ITO/HgTe/Ag-HgTe/Au detector structure. **b** Cross-sectional image of the HgTe CQDs detector using the FIB. **c** Band energy diagram.

between HgTe and Ag-HgTe NCs effectively prevents the electron from flowing to the opposite side. For the top electrode, Au is used owing to its function as an excellent back reflector against infrared radiation.

The performance of the photodiode device fabricated in Fig. 2 was examined at 78 and 130 K (Fig. 3a, b, Supplementary Fig. 12). The device offers a clear rectifying feature, proving that the built-in potential is well-formed at the junction between n- and p-doped materials. The rectification stability is shown in Supplementary Fig. 13, where the current density-voltage (J-V) curves are measured in various temperatures from 78 to 240 K. The rectifying feature remains distinct up to 150 K, but the leakage current increases when the temperature exceeds 150 K.

The following equation was used to calculate the responsivity:

$$R = \frac{J}{P} \quad (1)$$

where J is the photocurrent density, and P is the power density of the light source (21.7 mW cm<sup>-2</sup> at 300 °C blackbody). The highest responsivity was 0.31 and 0.58 A W<sup>-1</sup> at 78 K and 130 K, respectively. Considering the importance of a high-temperature operating photodetector, it is worth noting that the responsivity was higher at 130 K than at 78 K.

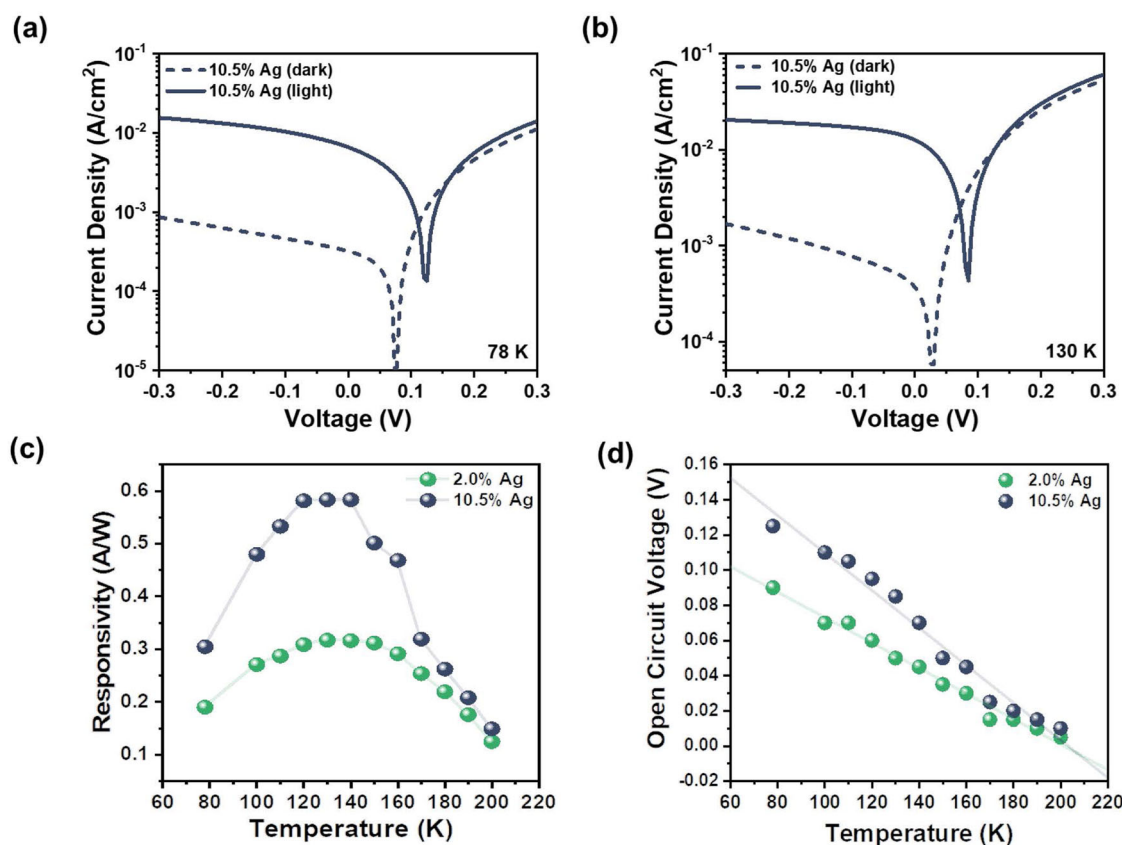


**Fig. 3 | Characterization of the HgTe CQDs detectors with different Ag content in the Ag-HgTe NCs layer.** A series of J-V characteristics under dark (dashed line) and light (300 °C blackbody radiation, solid line) at a 78 K and b 130 K. c Responsivities

and d open circuit voltage as a function of the operating temperature under 300 °C blackbody radiation.

### Silver doping control and its effect on the device performance

The Ag doping effect is further studied at various temperatures by controlling the Hg-to-Ag precursor ratio. The real Ag content in each Ag-HgTe NCs was analyzed by inductively coupled plasma-mass spectrometry (ICP-MS) and -optical emission spectrometry (ICP-OES). When the Hg-to-Ag precursor ratio is 1, the average atomic percent of Ag is 10.5%, while the Hg-to-Ag precursor ratio of 0.3 results in 2.0% of Ag. The atomic percentage of other elements is shown in Supplementary Fig. 14. Hereafter, we named '10.5% Ag' for Ag-HgTe which contains 10.5% of Ag and '2.0% Ag' for Ag-HgTe which contains 2.0% of Ag. It should be noted that synthesis and fabrication methods were same and the Hg-to-Ag precursor ratio was the only variable.

Figure 3c presents the temperature-dependent open circuit voltage ( $V_{OC}$ ) of devices fabricated with 2.0% and 10.5% Ag-HgTe NCs. The  $V_{OC}$  shows a linear relationship with temperature given by

$$V_{OC} = \frac{E_a}{q} - \frac{nKT}{q} \ln\left(\frac{J_{00}}{J_{SC}}\right) \quad (2)$$

where  $E_a$  is the activation energy,  $n$  is the diode ideality factor,  $k$  is the Boltzmann constant,  $T$  is the temperature,  $J_{SC}$  is the photocurrent, and  $J_{00}$  is the reverse saturation current prefactor<sup>25,37</sup>. At 0 K,  $V_{OC}$  should be close to the bandgap energy, while the  $V_{OC}$  for 10.5% Ag and 2.0% Ag-HgTe devices shows lower values than the bandgap energy of HgTe NCs ( $\sim 0.36$  eV). It implies that the  $V_{OC}$  deficit originated from the energy disorder, which broadens the state density and nonradiative recombination. According to Eq. 1, the higher  $J_{SC}$  induces its higher  $V_{OC}$ , demonstrated in the experimental results between 10.5% Ag and 2.0% Ag-HgTe devices (Supplementary Fig. 12).

Temperature-dependent responsivity was measured for devices fabricated with 10.5% Ag and 2.0% Ag-HgTe NCs (Fig. 3d). The 10.5% Ag-HgTe NCs show higher performance compared to the 2.0% Ag-HgTe NCs, where the gap in responsivity was approximately twice at 120–140 K. To investigate the difference between 2.0% and 10.5% Ag-HgTe NCs, the ultraviolet photoelectron spectroscopy (UPS) was conducted to identify the Fermi level position (Supplementary Fig. 11). While the Fermi level and the valence band edge were 0.22 eV apart in 10.5% Ag-HgTe NCs, those of 2.0% Ag-HgTe NCs were 0.32 eV apart, which indicates the Fermi level of 10.5% Ag-HgTe NCs is much closer to the valence band compared to 2.0% Ag-HgTe NCs. The UPS results corroborate that the high Ag content leads to a higher p-type character. In addition, when the Hg-to-Ag precursor ratio varied in detail from 1:0.3 to 1:1, the responsivity was enhanced as the Ag precursor ratio increased (Supplementary Fig. 15). The strong p-doping of Ag-HgTe NCs plays a vital role in forming the suitable built-in potential, resulting in a significant performance improvement. Since the highest performance was obtained with 10.5% Ag, it was used as p-type material for further optimization.

### Ligand control and its effect on the device performance

Along with the doping density that determines the intrinsic band level of the material, the ligand exchange, the essential step for facilitating the charge transport, substantially modifies the band alignment in the device<sup>26,38,39</sup>. Since the NCs are sensitive to the surface, the different interactions with the atoms constituting each ligand change the surface dipole moment, which shifts the conduction or valence band positions concerning the environmental Fermi level. The ligand also can serve as a filler for the defect site, passivating the trap sites and eventually changing the electron density<sup>40,41</sup>. It has been reported that changing only the ligand type causes almost 1 eV of a

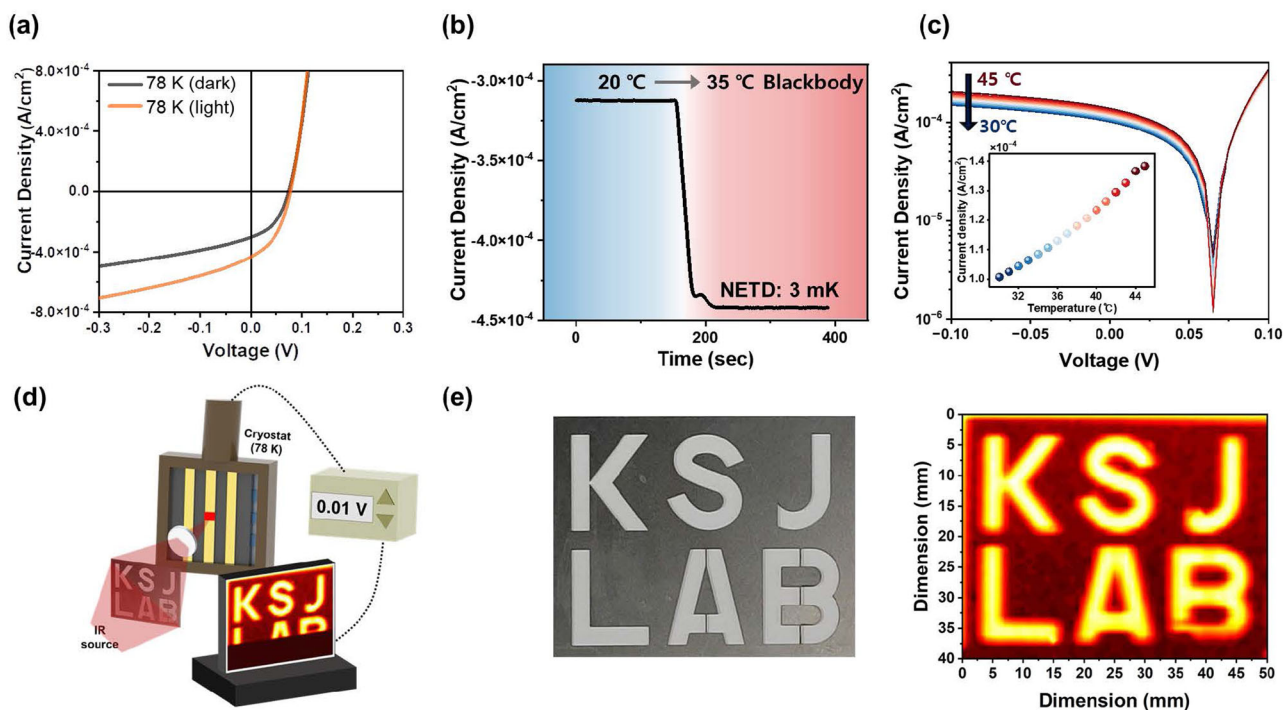


**Fig. 4 | Analysis on the thermal resolution.** **a** J-V characteristics under weak blackbody radiation intensity of 20 °C and 35 °C at 78 K. **b** Time-dependent current density curve derived from the blackbody radiation difference. The data were collected at a constant voltage of  $-0.005$  V, close to 0 V. **c** J-V curves under the

blackbody radiation from 30 to 45 °C. (Inset: Current density at 0 V with various temperatures). **d** Schematic of the imaging measurement set-up. **e** The actual image (left) and the corresponding thermal image captured by the HgTe CQDs detector at 78 K (right).

shift in the band level<sup>39</sup>. Furthermore, the ligand substantially influences the performance and stability of the device by affecting the film uniformity and the surface of the NCs layer. Although conventional EDT has shown its superiority by realizing promising performance<sup>42–44</sup>, the high reactivity of short alkyl thiol ligands could cause a rapid and aggressive exchange process, resulting in the partially aggregated film. Moreover, organic molecules are vulnerable to oxidation and heat, which is directly related to the air stability and lifetime of the devices. Thus, it is necessary to investigate different ligands for better, long-lasting performance.

For comparison with the previous ligand, EDT, we chose 1,6-hexanedithiol (HDT) and cetyltrimethylammonium bromide (CTAB). HDT is expected to mitigate the aggressive exchange process due to its longer organic chain, contributing to the film uniformity. On the other hand, CTAB can offer more robust environmental stability to the NCs layer as inorganic ligands and better conductivity via enhancing the wavefunction overlap of NCs<sup>45–47</sup>. To verify the difference, all devices were fabricated by the same method using different ligands for the p-type material optimized above (10.5% Ag-HgTe NCs), and each responsivity was averaged by 21 devices.

Figure 4a,b shows the averaged responsivities and J-V curves of devices using three different ligands with the standard deviation. Surprisingly, the responsivity can be further improved as almost twice as high with CTAB compared to EDT. The specific detectivity of the CTAB-treated device is given by

$$D^* = R\sqrt{A}/N \quad (3)$$

where  $N$  is the spectral noise density ( $0.5 \text{ pA Hz}^{-1/2}$ ),  $R$  is the responsivity ( $0.58 \text{ A W}^{-1}$ ), and  $A$  is the area of the detector ( $1.05 \text{ mm}^2$ ). Based on the spectral noise density measurement (Supplementary Fig. 16), the highest specific detectivity was  $1.15 \times 10^{11}$  Jones at 130 K.

To explore what brings the difference, we conducted the UPS on the ligand-treated NCs films to scrutinize the band energy level (Supplementary Fig. 11). The films were fabricated at the same thickness as the devices for the exact comparison. The UPS spectra demonstrate that the energy level of the

EDT-treated Ag-HgTe NCs layers lies somewhat shallow, where the valence band is similar to that of the conduction band of the HgTe NCs layers. In contrast, the valence band of the CTAB-treated Ag-HgTe NCs layers (10.5% Ag) is 0.33 eV deeper than the conduction band of the HgTe NCs layers, which is more favorable for forming the p-n junction.

Besides the different band alignments, better responsivity is also attributable to more stable surface passivation by bromide atomic ligands. Unlike divalent ligands such as EDT and HDT that possibly render a negatively charged surface<sup>45</sup>, monovalent bromide ions can bind to each cation on the NCs surface, providing a charge-neutral surface. Thus, it contributes to effective defect passivation, hindering the undesired recombination paths. Moreover, bromide ligands exhibit a slower exchange rate than EDT while at the same time effectively reducing the interparticle spacing down to 0.1 nm shorter than that of EDT owing to the atomic composition<sup>45</sup>. It indicates that the NCs can form a less aggregated film with more conductivity that will lower the energy barrier for the electrons to move toward the electrode.

Despite the overall higher responsivity, the devices with the CTAB reveal a large standard deviation in responsivity among different devices. This can be attributed to the solid-state ligand exchange process, where alcohol is used to wash residual ligands. Since halides are vulnerable to protons, the alcohol-washing process can cause the desorption of halide ions on the NCs surface, forming the trap sites. However, it should be noted that even the lowest responsivity of devices using the CTAB outperforms the average responsivities of those using EDT and HDT, which shows the promising role of CTAB when the exchange process is further optimized. The HDT also exhibits relatively higher responsivity than the EDT, likely due to the mild ligand exchange rate. Nevertheless, the improvement is insignificant since a longer organic chain could form a higher energy barrier between the NCs, which reemphasizes the superior performance of the short atomic CTAB ligand. It also should be noted that the CTAB-treated devices show consistent rectification features through all cells in one device, demonstrating that CTAB treatment can render uniform ligand exchange (Supplementary Fig. 17).

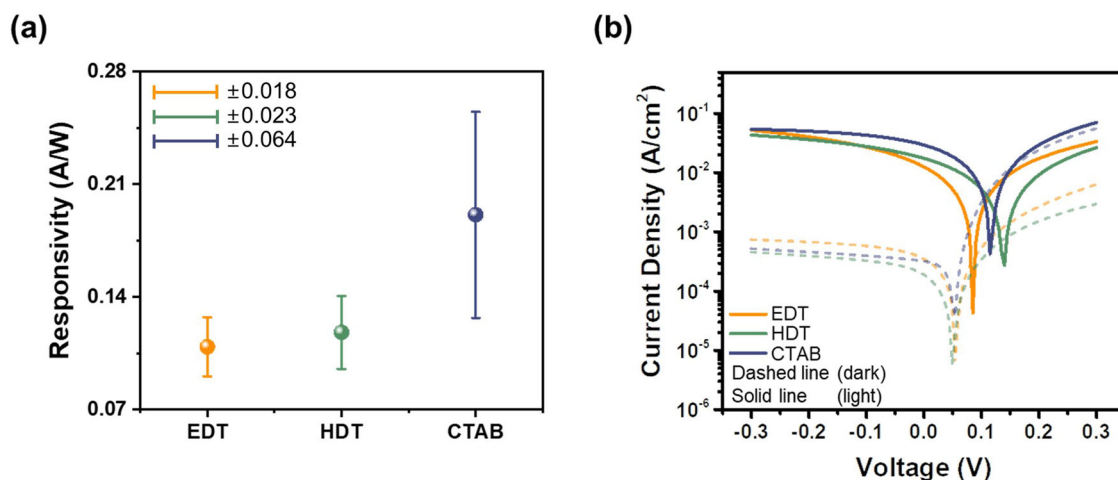


**Fig. 5 | The ligand-dependent photoresponse.** **a** Responsivity with various ligands used for the Ag-HgTe NCs layer (yellow, green, and blue lines in the legends represent the standard deviations) and the **b** current density of the detectors with different ligands at 78 K.

### Temperature resolution measurement and the thermal imaging

The noise equivalent temperature difference (NETD) of the infrared detector is an essential factor to show the sensitivity for the slight change in temperature<sup>48</sup>. The low NETD value leads to operating the infrared camera with a high thermal resolution. The CTAB-treated Ag-HgTe NCs device shows a noticeable difference in  $J_{SC}$  value under the blackbody radiation of 20 and 35 °C (Fig. 5a, b). The photocurrent with changing the blackbody radiation temperature is shown in Fig. 5b, and the NETD is calculated by

$$NETD = \frac{\Delta T}{SNR} = \frac{\Delta T}{\Delta J_s / J_n} \quad (4)$$

where  $\Delta T$  is the temperature difference,  $\Delta J_s$  is the measured photocurrent density difference between two blackbody radiation intensities, and  $J_n$  is the RMS noise calculated from the  $J_{SC}$  values at the specific temperature<sup>48</sup>.  $\Delta T$  is 15 °C.  $\Delta J_s$  is 0.13 mA cm<sup>-2</sup>, observed from the time-dependent current density curve.  $J_n$  of  $2.381 \times 10^{-8}$  A cm<sup>-2</sup> is calculated from the  $J_{SC}$  values at 20 °C. Here, the minimum and the average NETD values are 3 mK and 6 mK, respectively. We compared these values with previous reports on HgTe-based photodetectors in Supplementary Fig. 18 and Table 1, which shows a high temperature resolution of the device studied here. Considering the theoretical NETD equation<sup>48</sup>,

$$NETD \propto \frac{1}{D^* \sqrt{A}} \quad (5)$$

where  $A$  is the device area and  $D^*$  is the detectivity. The low NETD could be partially affected by the large area (1.05 mm<sup>2</sup>) of the device fabricated here. Since the NETD is inversely proportional to  $\sqrt{A}$  and the area of the device studied here is relatively large compared to those in other research, it is reasonable to show the NETD as low as 3 mK. Low NETD value was further demonstrated by the J-V curves where the responsivities were distinguished by 1 °C of blackbody radiation (Fig. 5c).

Along with the low NETD value, the high stability under the voltage and varying temperature is essential for practical use. We tested the stability of the device performance by a hundred times measurement under the bias voltage from -0.3 V to 0.3 V and temperatures varying from 78 K to 300 K. The measurement procedure is as follows: (1) At 78 K, the device was swept three times with different blackbody radiations (20 °C, 35 °C, 300 °C), and the same procedure was repeated at 150 K. Total 6 scans were measured. (2) The temperature was increased to RT (300 K) and lowered to 78 K again in the vacuum. (3) 1–2 steps were repeated 18 times, so 108 scans were swept in total. When the responsivity value of the first measurement is set to 100%, the device performance is maintained approximately up to ~80% even after

sweeping 103 times, suggesting good stability under varying voltages and temperatures (Supplementary Fig. 19).

Finally, we visually demonstrated the performance of the CTAB-treated Ag-HgTe detector by scanning the thermal image. The scanning image system for the infrared imaging of the CTAB-treated Ag-HgTe detector is shown in Fig. 5d, and details of the imaging set-up are summarized in the experimental part. The thermal imaging of the mask was obtained by the single pixel of the detector, and the image shows the clear features of the mask (Fig. 5e). The blackbody radiation that passed through the holes of the mask was projected to the detector, and the photocurrent generated by the pixel was recorded to construct the infrared image. The number of points to construct the 50 mm × 40 mm thermal image was 101 in horizontal and 81 in vertical directions. Since the p-CTAB-treated Ag-HgTe/n-HgTe QD detector can distinguish the thermal radiation difference of 3 mK, the HgTe CQD-based detector shows excellent potential for replacing the MCT or InSb-based epitaxial semiconductor detectors.

### Conclusions

In summary, we successfully fabricated the MWIR CQDs-based photodetector showing a high performance in NETD of 3 mK at 78 K. The p-doped Ag-HgTe NCs were synthesized by one-pot synthesis method. Using such facile synthesis methods, the silver doping ratio could be controlled, which makes the appropriate band alignment in the device. Also, with increasing the silver doping ratio, the p-type character of Ag-HgTe NCs was enhanced, and the responsivity reached 0.58 A W<sup>-1</sup> at 130 K. The ligand exchange, which determines the conductivity of the QD film, was a key to improving the device performance. Monovalent bromide ions passivated the surface of Ag-HgTe NCs well, preventing the aggregation of films. As a result, the p-CTAB-treated Ag-HgTe/n-HgTe QD device achieved a low NETD value compared to the previous HgTe CQD-based-photodetector. This is attributed to efficiently suppressing noise by fabricating well-distributed CQDs layers with extremely smooth surfaces of QDs layers and the large area of the device. The thermal image was successfully obtained by a single pixel of the device. The HgTe CQDs-based device results with Ag-HgTe p-type material indicate the great potential for applications in low-cost and high-sensitive MWIR thermal sensing cameras.

### Methods

#### HgTe NCs synthesis

1.5 mmol of HgCl<sub>2</sub> and 50 mL of OLAM were placed in a 200 mL three-neck flask, followed by degassing under vacuum (~100 mTorr) at 100 °C for 1 h. For the tellurium precursor stock solution (1 M TOP-Te), 10 mmol of tellurium powder was dissolved in 10 mL of TOP with vigorous stirring at 100 °C for 1 h in the glovebox. After the Hg precursor solution was degassed,

the temperature of the flask was set to 97 °C under an argon flow. 1.5 mL of 1 M TOP-Te solution was rapidly injected into the three-neck flask, and after the desired reaction time, 4 mL of DDT and 4 mL of TOP were injected with an ice bath quenching. The product solution was centrifuged with chloroform to remove the byproducts. The supernatant was precipitated with ethanol, and the precipitates were redispersed in chlorobenzene. The redispersed HgTe was added to a vial with didodecyldimethylammonium bromide (DDAB) and stirred for 45 minutes to remove the excess ligand.

### Ag-HgTe NCs synthesis

Ag-HgTe NCs were prepared with a similar method of HgTe NCs. The 0.5 or 1.5 mmol of AgCl powder, 1.5 mmol of HgCl<sub>2</sub>, and 50 mL of OLAM were dissolved in a 200 mL three-neck flask. After degassing, 4 mL of 1 M TOP-Te solution was quickly injected into the flask at 97 °C under argon gas. The reaction proceeded for 1 min and 30 s, followed by injection of ligand mixture solution (DDT and TOP) with an ice bath quenching. The precipitation process was same as HgTe NCs.

### Device fabrication

Sapphire substrates (11 mm × 11 mm) with a thickness of 0.65 mm. Indium tin oxide was sputtered over the substrates at 70 nm as an electrode. The ITO-sapphire substrate was cleaned by sonicating it with distilled water, chloroform, acetone, and IPA. The dried substrate was treated with 1% (v/v) MPTMS/toluene solution for 30 s and washed by IPA. 30 μL of HgTe NCs was dropped and spread over the overall surface of the substrate by handling. The NCs film was annealed at 50 °C, and then the film was immersed in an EDT/HCl/IPA (1:1:100 by volume). After ligand exchange, the film was washed by IPA 3 times. This process was repeated 3–7 times to fabricate the active layer film. For the p-type layer, 30 μL of Ag-HgTe NCs was used in the same method as the HgTe layer. EDT, HDT, and CTAB ligands were dissolved in IPA, respectively, to compare the ligand exchange effects. The process of the p-type layer was repeated 1–2 times. Finally, the Au electrode (80 nm) was deposited by a thermal evaporator.

### Fourier-transform infrared absorption

The FTIR absorption spectra were measured by a Nicolet iS10 FT-IR with a resolution of 0.482 cm<sup>-1</sup>.

### X-ray Diffraction

A Rigaku Ultima III X-ray diffractometer with graphite-monochromatized Cu K $\alpha$  ( $\lambda = 1.54056 \text{ \AA}$ ) was used to measure the XRD pattern. The irradiation power was 40 kV with 30 mA. The sampling width was 0.01°.

### High-resolution analytical transmission electron microscope

The morphology of HgTe and Ag-HgTe NCs was investigated by a Tecnai 20 model, which used 200 kV of acceleration voltage.

### X-ray photoelectron spectroscopy

The K-alpha Model with the monochromated Al X-ray sources (Al K $\alpha$  line: 1486.6 eV) was used to measure the XPS spectra. The XPS spectra were calibrated to the value of C 1s (284.8 eV). The atomic percent of NCs was investigated from the XPS spectra.

### Ultraviolet photoelectron spectroscopy

The UPS spectra were collected by a (Nexsa™ X-Ray Photoelectron Spectrometer) with the He(I) line with an energy of 21.22 eV. The energy step size was set to 0.050 eV.

### Focused Ion Beam

The cross-sectional specimen of the fabricated device was taken with a FEI Helios G5 UC focused ion beam.

### Field effect transistors

Heavily n-doped silicon wafer with a 300 nm thickness of SiO<sub>2</sub> was used as the substrate for the back-gated thin film transistors. After cleaning with the

organic solvents, Ti (5 nm)/Au (50 nm) interdigitated electrodes were thermally evaporated, and the wafer was diced into 3 cm × 3 cm. The channel width and length of the interdigitated electrodes were 5.28 mm and 10 μm, respectively. Each NC was drop-casted and annealed at 50 °C. The films were treated with the CTAB or HCl/EDT solution for the ligand exchange and washed by IPA. The process was repeated for 1–2 times. Transfer characteristics of the FET were measured with a semiconductor parameter analyzer (4200A-SCS).

### J-V measurement

For the electrical characterization of the device, the current density-voltage spectra were measured with a semiconductor parameter analyzer (4200A-SCS). The fabricated device was placed in a Janis ST-100 optical cryostat with a CaF<sub>2</sub> window to lower the operating temperature. A calibrated blackbody (Omega BB703, 300 °C) was used as the infrared illumination source to see the photoresponsivity of the device. The J<sub>SC</sub> value was defined as the current density value at 0 voltage.

### Noise spectral density measurement

For the noise spectral density measurement, the device was connected inside the cryostat and placed in the home-built Faraday cage to reduce exposure to external noise. The temperature of the cryostat was lowered to 78 K. Low-noise current preamplifier (Stanford Research Systems, SR570) was connected to the device to amplify the current signal to the voltage unit. For the frequency-dependent voltage RMS spectra, the FFT dynamic signal analyzer (Stanford Research Systems, SR785) was used.

### NETD measurement

The NETD was calculated from the time-dependent current density spectrum from a semiconductor parameter analyzer (4200A-SCS). A constant voltage of -0.005 V was applied to the device. During the measurement of 388 s, a total of 4097 scan points were measured. The blackbody radiation of 20 °C (home-built by the I3 system corporation) was maintained for 150 s and changed to 35 °C in 80 s. The RMS value was calculated from the current density records at 20 °C.

### Infrared image measurement

A single pixel of the fabricated device was used to scan the corresponding infrared image of the shadow mask. The mask was placed on the X-Y scanner, and the blackbody radiation (Thorlab, SLS303) passed through the holes of the mask. Since the device was operated with low-temperature blackbody radiation, the shutter of SLS303 was used with a closed state. A scanning lens was mounted in front of the cryostat and projected the image across the detector. The device was operated at 78 K with a constant voltage of 0.01 V from a low-noise current preamplifier (Stanford Research Systems, SR570). The photocurrent value was recorded by moving the mask with an X-Y scanner. The number of points to construct the 50 mm × 40 mm thermal image was 101 in horizontal and 81 in vertical directions.

### Supporting information

ICP-MS results, XPS spectra, TEM images with EDS mapping, FT-IR spectra, Cross-sectional FIB image, UPS spectra, Drain current-gate voltage characteristic, J-V curves, Responsivity ratio, Noise density spectrum, NETD value comparison.

### Data availability

All data that support the findings of this study are available within the article and its Supplementary Figs. and table.

Received: 18 November 2023; Accepted: 8 April 2024;

Published online: 24 April 2024

### References

1. Itsuno, A. M., Phillips, J. D. & Velicu, S. Mid-wave infrared HgCdTe nBn photodetector. *Appl. Phys. Lett.* **100**, 161102 (2012).

2. Ariyawansa, G., Duran, J., Reyner, C. & Scheihing, J. InAs/InAsSb strained-layer superlattice mid-wavelength infrared detector for high-temperature operation. *Micromachines* **10**, 806 (2019).
3. Sharabani, Y., Paltiel, Y., Sher, A., Raizman, A. & Zussman, A. InAsSb/GaSb heterostructure based mid-wavelength-infrared detector for high temperature operation. *Appl. Phys. Lett.* **90**, 232106 (2007).
4. Kovalenko, M. V. et al. Colloidal HgTe nanocrystals with widely tunable narrow band gap energies: From telecommunications to molecular vibrations. *J. Am. Chem. Soc.* **128**, 3516–3517 (2006).
5. Guo, Q. et al. Black phosphorus mid-infrared photodetectors with high gain. *Nano Lett.* **16**, 4648–4655 (2016).
6. Schwanninger, R. et al. Highly responsive mid-infrared metamaterial enhanced heterostructure photodetector formed out of sintered PbSe/PbS colloidal quantum dots. *ACS Appl. Mater. Interfaces* **15**, 10847–10857 (2023).
7. Zhang, H. et al. Material perspective on HgTe nanocrystal-based short-wave infrared focal plane arrays. *Chem. Mater.* **34**, 10964–10972 (2022).
8. Zhang, S. et al. Direct optical lithography enabled multispectral colloidal quantum-dot imagers from ultraviolet to short-wave infrared. *ACS Nano* **16**, 18822–18829 (2022).
9. Zhang, S. et al. Spray-stencil lithography enabled large-scale fabrication of multispectral colloidal quantum-dot infrared detectors. *Adv. Mater. Technol.* **7**, 2101132 (2022).
10. Yang, J. et al. Ligand-engineered HgTe colloidal quantum dot solids for infrared photodetectors. *Nano Lett.* **22**, 3465–3472 (2022).
11. Peterson, J. C. & Guyot-Sionnest, P. Room-temperature 15% efficient mid-infrared HgTe colloidal quantum dot photodiodes. *ACS Appl. Mater. Interfaces* **15**, 19163–19169 (2023).
12. Lhuillier, E. et al. Infrared photodetection based on colloidal quantum-dot films with high mobility and optical absorption up to THz. *Nano Lett.* **16**, 1282–1286 (2016).
13. Park, M., Choi, D., Choi, Y., Shin, H. & Jeong, K. S. Mid-infrared intraband transition of metal excess colloidal Ag<sub>2</sub>Se nanocrystals. *ACS Photonics* **5**, 1907–1911 (2018).
14. Kim, G., Choi, D., Eom, S. Y., Song, H. & Jeong, K. S. Extended short-wavelength infrared photoluminescence and photocurrent of nonstoichiometric silver telluride colloidal nanocrystals. *Nano Lett.* **21**, 8073–8079 (2021).
15. An, M. N. et al. Room temperature synthesis of self-doped silver selenide quantum dots sensitive to mid-infrared light. *ACS Appl. Nano Mater.* **6**, 22488–22495 (2023).
16. Bera, R., Choi, D., Jung, Y. S., Song, H. & Jeong, K. S. Intraband transitions of nanocrystals transforming from lead selenide to self-doped silver selenide quantum dots by cation exchange. *J. Phys. Chem. Lett.* **13**, 6138–6146 (2022).
17. Choi, D. & Jeong, K. S. Midwavelength infrared photoluminescence and lasing of tellurium elemental solid and microcrystals. *J. Phys. Chem. Lett.* **10**, 4303–4309 (2019).
18. Bera, R., Kim, G., Choi, D., Kim, J. & Jeong, K. S. Beyond the bandgap photoluminescence of colloidal semiconductor nanocrystals. *J. Phys. Chem. Lett.* **12**, 2562–2569 (2021).
19. Son, J., Choi, D., Park, M., Kim, J. & Jeong, K. S. Transformation of colloidal quantum dot: from intraband transition to localized surface plasmon resonance. *Nano Lett.* **20**, 4985–4992 (2020).
20. Kim, J., Choi, D. & Jeong, K. S. Self-doped colloidal semiconductor nanocrystals with intraband transitions in steady state. *Chem. Commun.* **54**, 8435–8445 (2018).
21. Choi, D. et al. Major electronic transition shift from bandgap to localized surface plasmon resonance in Cd<sub>x</sub>Hg<sub>1-x</sub>Se alloy nanocrystals. *Chem. Mater.* **29**, 8548–8554 (2017).
22. Yoon, B., Jeong, J. & Jeong, K. S. Higher quantum state transitions in colloidal quantum dot with heavy electron doping. *J. Phys. Chem. C.* **120**, 22062–22068 (2016).
23. Keuleyan, S., Lhuillier, E., Brajuskovic, V. & Guyot-Sionnest, P. Mid-infrared HgTe colloidal quantum dot photodetectors. *Nat. Photonics* **5**, 489–493 (2011).
24. Guyot-Sionnest, P. & Roberts, J. A. Background limited mid-infrared photodetection with photovoltaic HgTe colloidal quantum dots. *Appl. Phys. Lett.* **107**, 253104 (2015).
25. Ackerman, M. M., Tang, X. & Guyot-Sionnest, P. Fast and sensitive colloidal quantum dot mid-wave infrared photodetectors. *ACS Nano* **12**, 7264–7271 (2018).
26. Chen, M. et al. HiGh Carrier Mobility in HgTe quantum dot solids improves mid-IR photodetectors. *ACS Photonics* **6**, 2358–2365 (2019).
27. Abadie, C. et al. Helmholtz resonator applied to nanocrystal-based infrared sensing. *Nano Lett.* **22**, 8779–8785 (2022).
28. Liu, Y. et al. Dependence of carrier mobility on nanocrystal size and ligand length in PbSe nanocrystal solids. *Nano Lett.* **10**, 1960–1969 (2010).
29. Lhuillier, E. & Guyot-Sionnest, P. Recent progresses in mid infrared nanocrystal optoelectronics. *IEEE J. Sel. Top. Quantum Electron.* **23**, 1–8 (2017).
30. Chen, M. et al. Magnetoresistance of high mobility HgTe quantum dot films with controlled charging. *J. Mater. Chem. C.* **10**, 13771–13777 (2022).
31. Chu, A. et al. HgTe nanocrystals for SWIR detection and their integration up to the focal plane array. *ACS Appl. Mater. Interfaces* **11**, 33116–33123 (2019).
32. Liu, F. et al. Near-infrared emission from tin-lead (Sn-Pb) alloyed perovskite quantum dots by sodium doping. *Angew. Chem.* **132**, 8499–8502 (2020).
33. Xia, K., Fei, G. T., Xu, S. H., Gao, X. D. & Liang, Y. F. Hot-injection synthesis of HgTe nanoparticles: Shape control and growth mechanisms. *Inorg. Chem.* **62**, 13632–13638 (2023).
34. Liao, L. et al. Multifunctional CuO nanowire devices: P-type field effect transistors and CO gas sensors. *Nanotechnology* **20**, 085203 (2009).
35. Jagtap, A. et al. Short wave infrared devices based on HgTe nanocrystals with air stable performances. *J. Phys. Chem. C.* **122**, 14979–14985 (2018).
36. Chen, M. & Guyot-Sionnest, P. Reversible electrochemistry of mercury chalcogenide colloidal quantum dot films. *ACS Nano* **11**, 4165–4173 (2017).
37. Chuang, C.-H. M. et al. Open-circuit voltage deficit, radiative sub-bandgap states, and prospects in quantum dot solar cells. *Nano Lett.* **15**, 3286–3294 (2015).
38. Xue, X. et al. High-operating-temperature mid-infrared photodetectors via quantum dot gradient homojunction. *Light Sci. Appl.* **12**, 2 (2023).
39. Brown, P. R. et al. Energy level modification in lead sulfide quantum dot thin films through ligand exchange. *ACS Nano* **8**, 5863–5872 (2014).
40. Voznyy, O. et al. A charge-orbital balance picture of doping in colloidal quantum dot solids. *ACS Nano* **6**, 8448–8455 (2012).
41. Ning, Z., Dong, H., Zhang, Q., Voznyy, O. & Sargent, E. H. Solar cells based on inks of N-type colloidal quantum dots. *ACS Nano* **8**, 10321–10327 (2014).
42. Luther, J. M. et al. Structural, optical, and electrical properties of self-assembled films of pbse nanocrystals treated with 1,2-ethanedithiol. *ACS Nano* **2**, 271–280 (2008).
43. Sergeeva, K. A. et al. Ultrafast charge carrier dynamics and transport characteristics in HgTe quantum dots. *J. Phys. Chem. C.* **126**, 19229–19239 (2022).
44. Livache, C. et al. Band edge dynamics and multiexciton generation in narrow band gap HgTe nanocrystals. *ACS Appl. Mater. Interfaces* **10**, 11880–11887 (2018).
45. Tang, J. et al. Colloidal-quantum-dot photovoltaics using atomic-ligand passivation. *Nat. Mater.* **10**, 765–771 (2011).



46. Semonin, O. E., Luther, J. M. & Beard, M. C. Quantum dots for next-generation photovoltaics. *Mater. Today* **15**, 508–515 (2012).
47. Liu, M., Wang, Y.-Y., Liu, Y. & Jiang, F.-L. Thermodynamic implications of the ligand exchange with alkylamines on the surface of CdSe quantum dots: The importance of ligand–ligand interactions. *J. Phys. Chem. C* **124**, 4613–4625 (2020).
48. Tang, X., Ackerman, M. M. & Guyot-Sionnest, P. Thermal imaging with plasmon resonance enhanced HgTe colloidal quantum dot photovoltaic devices. *ACS Nano* **12**, 7362–7370 (2018).

### Acknowledgements

This research was supported by the Challengeable Future Defense Technology Research and Development Program through the Agency for Defense Development (ADD) funded by the Defense Acquisition Program Administration (DAPA) in 2024 (No.912903601), the National Research Foundation of Korea (NRF) grant funded by the Korean government (Ministry of Science and ICT) (2021R1A2C2092053 and 2022M3H4A1A03076626), and a National Research Foundation of Korea (NRF) funded by the Ministry of Education (2022R111A1A01065661).

### Author contributions

H. S., S. Y. E., and G. K. contributed equally to this study. K. S. J. designed the experiments, H. S., S. Y. E., G. K., and J. B. prepared NCs samples and fabricated the devices, Y. S. J., D. C., G. S. K., J. H. L., H. S. K., and S. H. measured and analyzed the devices performance, G. W. S. and G. W. H. conducted the FET measurements, S. B., and W. K provided advice, and H. S., S. Y. E., G. K., and K. S. J. wrote the manuscript with input from all the authors.

### Competing interests

The authors declare no competing interests.

### Additional information

**Supplementary information** The online version contains supplementary material available at <https://doi.org/10.1038/s43246-024-00499-z>.

**Correspondence** and requests for materials should be addressed to Kwang Seob Jeong.

**Peer review information** *Communications Materials* thanks the anonymous reviewers for their contribution to the peer review of this work. Primary Handling Editors: Klaas-Jan Tielrooij and Aldo Isidori.

**Reprints and permissions information** is available at <http://www.nature.com/reprints>

**Publisher's note** Springer Nature remains neutral with regard to jurisdictional claims in published maps and institutional affiliations.

**Open Access** This article is licensed under a Creative Commons Attribution 4.0 International License, which permits use, sharing, adaptation, distribution and reproduction in any medium or format, as long as you give appropriate credit to the original author(s) and the source, provide a link to the Creative Commons licence, and indicate if changes were made. The images or other third party material in this article are included in the article's Creative Commons licence, unless indicated otherwise in a credit line to the material. If material is not included in the article's Creative Commons licence and your intended use is not permitted by statutory regulation or exceeds the permitted use, you will need to obtain permission directly from the copyright holder. To view a copy of this licence, visit <http://creativecommons.org/licenses/by/4.0/>.

© The Author(s) 2024